

The variability, structure and energy conversion of the northern hemisphere traveling waves simulated in a Mars general circulation model



Huiqun Wang^{a,*}, Anthony D. Toigo^b

^a Smithsonian Astrophysical Observatory, 60 Garden Street, Cambridge, Massachusetts 02138, United States

^b Johns Hopkins University Applied Physics Laboratory, Laurel, Maryland 20723, United States

ARTICLE INFO

Article history:

Received 12 November 2014

Revised 23 January 2016

Accepted 1 February 2016

Available online 11 February 2016

Keywords:

Atmospheres, dynamics

Mars, atmosphere

Mars

ABSTRACT

Investigations of the variability, structure and energetics of the $m = 1–3$ traveling waves in the northern hemisphere of Mars are conducted with the MarsWRF general circulation model. Using a simple, annually repeatable dust scenario, the model reproduces many general characteristics of the observed traveling waves. The simulated $m = 1$ and $m = 3$ traveling waves show large differences in terms of their structures and energetics. For each representative wave mode, the geopotential signature maximizes at a higher altitude than the temperature signature, and the wave energetics suggests a mixed baroclinic-barotropic nature. There is a large contrast in wave energetics between the near-surface and higher altitudes, as well as between the lower latitudes and higher latitudes at high altitudes. Both barotropic and baroclinic conversions can act as either sources or sinks of eddy kinetic energy. Band-pass filtered transient eddies exhibit strong zonal variations in eddy kinetic energy and various energy transfer terms. Transient eddies are mainly interacting with the time mean flow. However, there appear to be non-negligible wave-wave interactions associated with wave mode transitions. These interactions include those between traveling waves and thermal tides and those among traveling waves.

© 2016 Elsevier Inc. All rights reserved.

1. Introduction

Traveling waves are common in the martian atmosphere. They are associated with substantial eddy momentum and heat fluxes, and are closely related to the martian dust cycle (Barnes, 1980, 1981; Barnes et al., 1993; Wilson et al., 2002; Wang et al., 2003, 2013; Banfield et al., 2004; Hinson and Wang, 2010). Traveling wave behavior can be characterized by using a handful of representative wave modes with well-defined zonal wavenumbers and wave periods. The dominant wave mode often changes rapidly with time – a phenomenon called “wave mode transition” (Collins et al., 1996). Analysis of the Mars Global Surveyor (MGS) Thermal Emission Spectrometer (TES) temperature data showed that wave mode transitions near the surface were common among zonal wavenumbers $m = 1, 2$ and 3 traveling waves (Banfield et al., 2004). The $m = 3$ traveling waves in the northern hemisphere show a positive correlation with the occurrences of frontal/flushing dust storms (Wang et al., 2003, 2005; Wang, 2007; Hinson and Wang, 2010; Hinson et al., 2012; Wang et al., 2013). Therefore, wave mode

transitions into and out of the $m = 3$ traveling waves are directly relevant to the martian dust cycle.

Wang et al. (2013) examined the strength, seasonality and dynamics of the zonal wavenumber $m = 3$ traveling waves simulated by the MarsWRF General Circulation Model (GCM). That study focused on the multi-year mean behavior. This paper builds on that work by analyzing the variability, with an emphasis on wave mode transitions, especially those involving the $m = 3$ traveling waves. In this context, the structures and energy conversions of the $m = 1–3$ traveling waves are examined. We are not studying waves with higher zonal wavenumbers, as Banfield et al. (2004) did not find them to be particularly strong in the MGS TES observations. We are interested in short wave period ($P \leq 15$ sols or so) traveling waves in the northern hemisphere since these are the waves most closely related to frontal/flushing dust storms (e.g., Hinson et al., 2012).

In Section 2, we briefly analyze the variability of traveling waves in a data assimilation product – the Mars Analysis Correction Data Assimilation (MACDA). This provides a base for assessing the variability simulated in our model. In Section 3, we introduce the MarsWRF model used in the rest of this paper. In Section 4, we present the simulated variability and make qualitative comparisons with the MACDA results. In Section 5, we investigate the structures

* Corresponding author. Tel.: +16174962268.

E-mail address: hwang@cfa.harvard.edu (H. Wang).

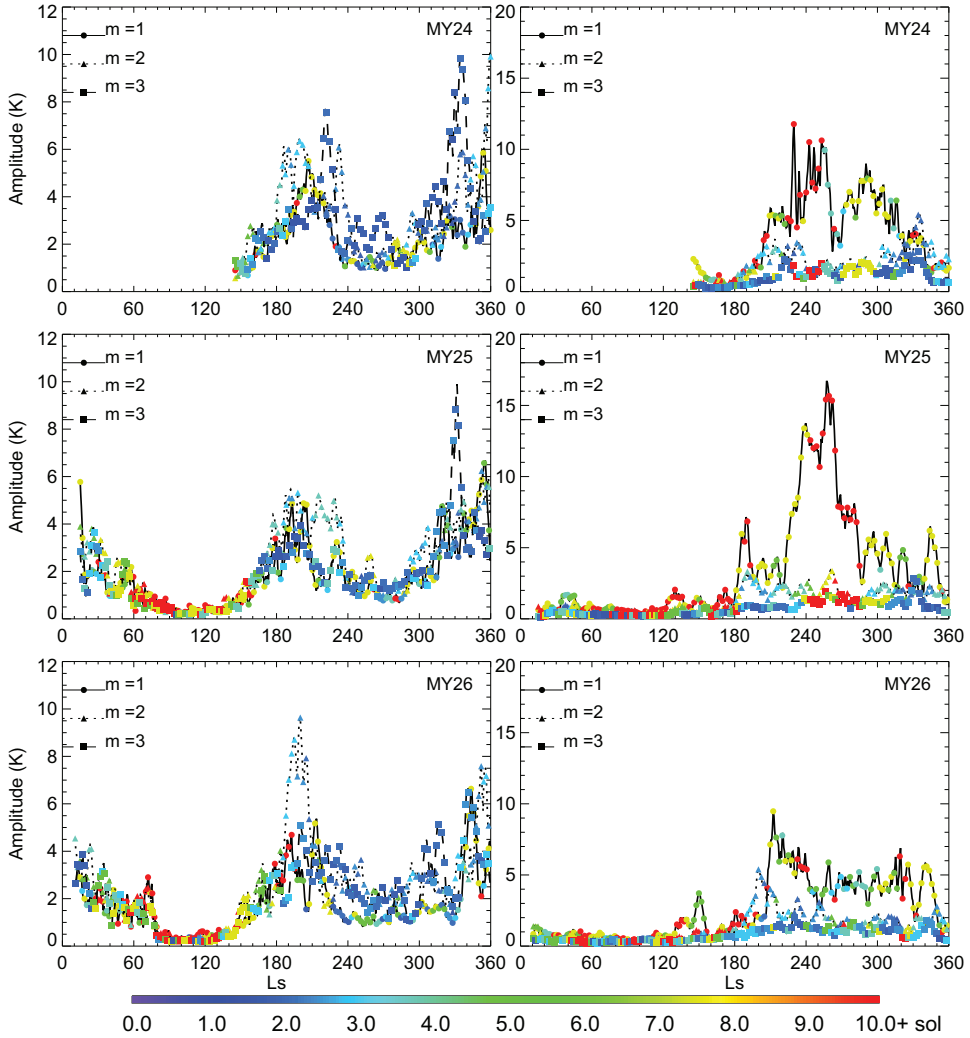


Fig. 1. The maximum amplitude of the northern hemisphere zonal wavenumber $m = 1$ (solid line with dots), $m = 2$ (dotted line with triangles) and $m = 3$ (dashed line with squares) eastward traveling waves derived from the MACDA temperature data (in K) as a function of L_s for Mars Year (MY) 24 (top row), 25 (middle row) and 26 (bottom row), respectively. The left column is for $\sigma \sim 0.9$ ($h \sim 1$ km) and the right column is for $\sigma \sim 0.04$ ($h \sim 35$ km). The colors of the symbols indicate the wave periods (sol) of the corresponding wave modes. For clarity, all points for each zonal wavenumber are connected by a line, but symbols are over-plotted every 4th point.

of representative wave modes that are commonly involved in wave mode transitions. The focus on individual wave modes is different than that of Barnes et al. (1993) and Kavulich et al. (2013), which was on the ensemble of transient eddies in their models. In Section 6, we examine the energetics of simulated traveling waves, focusing on the baroclinic, barotropic, and non-linear wave-wave interaction terms. In Section 7, we summarize our main results.

2. Analysis of a data assimilation product

We investigate wave mode transitions by extracting traveling waves from the MACDA v1.0 database (Montabone et al., 2014). This database is based on an assimilation of the MGS TES observations into the UK-LMD Mars GCM. It has a 5° latitude $\times 5^\circ$ longitude resolution and 25 terrain-following σ levels (where $\sigma = p/p_s$, p is atmospheric pressure and p_s is surface pressure). We perform a space-time Fourier spectral analysis using a running 15-sol window at 1-sol interval for each model latitude and σ level. Both the mean and the linear trend for each running window are removed before spectral analysis. Since we are interested in the short period traveling waves, we select a 15-sol window to filter out waves with longer wave periods. Our subsequent analyses go through the following steps. First, for each σ level, latitude, and zonal wavenumber, we search the wave period (P) space within

the $1.6 < P \leq 15$ sols range to find the wave mode with the largest amplitude. We will refer to the corresponding wave mode as the dominant wave mode. Then, for each σ level and zonal wavenumber, we find the maximum amplitude over all latitudes within the 0° – 90° N range. This amplitude and its associated wave period are plotted in Fig. 1 for the $m = 1, 2$ and 3 eastward traveling waves in the temperature field at MACDA's $\sigma \sim 0.90$ ($h \sim 1$ km, assuming a 10.8 km scale height) and $\sigma \sim 0.040$ ($h \sim 35$ km) vertical levels for Mars Year 24–26.

The left column of Fig. 1 shows that the low altitudes ($\sigma \sim 0.90$) in the northern hemisphere exhibit strong traveling waves from the fall to the spring before and after the northern winter solstice. During these seasons, there are apparent wave mode transitions among the $m = 1$ ($P \sim 7.5$ sols), $m = 2$ ($P \sim 3$ – 4 sols) and $m = 3$ ($P \sim 2$ – 3 sols) waves. As an example, Fig. 1 shows a transition from an $m = 2$ to $m = 1$ to $m = 3$ and to $m = 2$ during the pre-solstice time period (L_s 180°–240°) of Mars Year 24. Hinson et al. (2012) found that the transitions into and out of the $m = 3$ traveling waves influenced the occurrence of flushing dust storms and that the intermittence of the $m = 3$ waves played an important role in the annual dust cycle on Mars.

The right column of Fig. 1 shows that the $m = 1$ traveling waves are usually much stronger than the others at high altitudes ($\sigma \sim 0.040$) during $L_s = 180^\circ$ – 360° . The wave periods of the $m = 1$

waves switch among $P = 3.75$ sols, 7.5 sols, and 15 sols. This behavior is quite different from that of the low altitudes. Lewis et al. (2016) also noticed a contrast between the lower and higher atmosphere in a study of the same MACDA data set. In an analysis of the MGS TES temperature data, Wilson et al. (2002) reported a rapid wave mode transition from a slow ($P \sim 20$ sols) to a fast ($P \sim 6\text{--}7$ sol) $m = 1$ eastward traveling wave in the middle atmosphere in MY 24.

A part of the variability shown in Fig. 1 is due to the internal dynamics of the martian atmosphere, and the other part is due to the inter-annual variability of dust distribution (Wilson et al., 2002; Banfield et al., 2004; Lewis et al., 2016). For example, Wilson et al. (2002) showed that the wave periods of the dominant traveling waves changed during the course of a decaying dust storm. As can be seen from the L_s versus latitude distributions of dust optical depth in Smith (2004) and Montabone et al. (2015), major (hemispheric or global scale) dust storms occurred during different L_s periods in each Mars year. While the influence of major dust storms on traveling waves is an important part in understanding the variability of traveling waves, the inter-annual variability of these dust storms makes traveling waves more complicated to study in multi-annual simulations. Instead, it is useful to study traveling waves under an annually repeatable dust scenario, as this eliminates the variability in wave behavior due to changes in the underlying dust distribution. In Sections 4–6, we present the results from multi-year outputs of a MarsWRF simulation which used an annually repeatable dust distribution.

3. Model

The MarsWRF model used in this paper (Richardson et al., 2007; Toigo et al. 2012) is the same as that described in Wang et al. (2013). It has a 5° latitude $\times 5^\circ$ longitude horizontal resolution and 40 terrain-following vertical η levels between the surface and an upper boundary at about 5.7 mPa ($\eta = (p - p_t)/(p_s - p_t)$, where p is the hydrostatic pressure, p_s is the surface pressure, and p_t is the pressures at the model top, see Laprise, 1992). Since our chosen value for p_t is about 5 orders of magnitude smaller than p_s , η is essentially equivalent to the standard pressure-based vertical coordinate, σ ($=p/p_s$). The model physics parameterizations include radiative transfer for CO₂ and dust, CO₂ surface condensation and sublimation, surface layer, and planetary boundary layer, but in these simulations there is no explicit modeling of cloud micro-physics (Wang et al., 2013). The model employs a yearly repeatable dust distribution that is modified from the Mars Climate Database (MCD) “MGS dust scenario” (Montmessin et al., 2004).

We use a modified MCD “MGS dust scenario” since Wang et al. (2013) found that the MarsWRF simulation using the standard “MGS dust scenario” produced much weaker $m = 3$ traveling waves in the northern hemisphere when compared to observations. Capturing a better representation of the $m = 3$ traveling waves is important as these waves play an important role in the near-surface variability of temperature and winds and are closely related to flushing dust storms which are frequently involved in major dust storm development (Wang et al., 2003, 2005, 2013; Hinson and Wang, 2010; Hinson et al., 2012). Kavulich et al. (2013) noted that the GFDL Mars GCM with the Mars Year 24–25 dust distribution also underrepresented the $m = 3$ traveling waves in the northern hemisphere though some earlier models did not exhibit this behavior (Wang et al., 2003; Basu et al., 2006).

One way to enhance the strength of the northern hemisphere $m = 3$ traveling waves over that of the standard “MGS dust scenario” in our model is through the introduction of additional dust in the vicinity of the north polar cap (Wang et al., 2013). Image observations showed frequent dust storms at the polar cap edge (Cantor et al., 2001; Wang et al., 2005; Wang, 2007), which serves

as a motivation for prescribing additional dust there. In this paper, we include additional dust between 45°N and 75°N during L_s $180^\circ\text{--}360^\circ$, and label this simulation as “Simulation A”. The column opacity (τ) of the additional dust (beyond that prescribed in the “MGS dust scenario”) at the 7 mb reference level as a function of latitude (φ) follows a half-cosine curve that peaks at 60°N :

$$\tau(\varphi) = 2 \cdot \cos\left(\frac{\varphi - 60^\circ}{30^\circ}\pi\right), \quad 45^\circ < \varphi < 75^\circ. \quad (1)$$

The additional dust is zonally uniform at the 7 mb reference level and scales with surface pressure. The vertical dust distribution follows the same prescription as that in the standard “MGS dust scenario”. The distribution of dust in “Simulation A” is simplified and does not include any major dust storms. However, it improves the results for traveling waves, especially for zonal wavenumber $m = 3$ (Wang et al., 2013). In this paper, the model runs for 10 Mars years and outputs every 2 “hours” (i.e., 1/12 of a sol). The output from the last 9 years is used for our analyses.

It should be noted that polar hood clouds were also found to substantially increase the strength of transient eddies in GCMs (Mulholland et al., 2016). While most dust storms at northern high latitudes are concentrated near the edge of the polar cap (Cantor et al., 2001), polar hood clouds extend to the pole (Benson et al., 2011). To be more consistent with the position of the cap edge dust storms, the additional dust has been prescribed between 45°N and 75°N in this paper. Spacecraft images have shown that dust storms often co-exist with clouds in the polar region (Wang and Ingersoll, 2002). Thus, our prescription of extra dust in this region may also act as a proxy for the effect of polar clouds. Due to the cold surface near the winter polar vortex edge and the low height of cap edge dust storms (Määttänen et al., 2013), the dust optical depths derived from MGS TES and Mars Reconnaissance Orbiter (MRO) Mars Climate Sounder (MCS) data may underestimate the extent and amplitude of dust in the winter polar region. In our idealized experiment, we may be serendipitously including an effect of the combination of both aerosols, but without more detailed observations, it is difficult to estimate a contribution from each. Our goal, however, remains to analyze the structures and dynamics of traveling waves simulated by MarsWRF and not to exactly reproduce the observed aerosol distribution.

4. Variability

Wang et al. (2013) performed a space-time Fourier analysis using a 10-sol running analysis window (evaluated every 5 sols) to extract the amplitudes and phases of various waves for each latitude and vertical level. In that paper, the wave amplitudes for each zonal wavenumber (at each latitude) were first averaged in the wave frequency space corresponding to the $1.4 \leq P \leq 10$ sols wave period range. Then, these amplitudes (at each wavenumber and latitude) were binned in solar longitude with a 5° bin (spanning $360^\circ \times 9$ years of time). Finally, all bins with a solar longitude of the same time of year were averaged across 9 simulation years to produce a multi-annual, multi-frequency average for each zonal wavenumber and latitude at every 5° of solar longitude. In the left column of Fig. 2, we follow this method to examine the average amplitude of the $1.6 \leq P \leq 10$ sols traveling waves of “Simulation A”. To maintain consistency amongst all analysis in this paper, we have used a lower cutoff of 1.6 sols; however, our conclusions are insensitive to the choice between 1.4 sols and 1.6 sols for the lower cutoff.

Since the width of the spectral peak of the $m = 3$ traveling waves as a function of frequency is narrow ($f = 1/P, \sim 1/3 \text{ sol}^{-1} \text{--} 1/2 \text{ sol}^{-1}$), an average taken over a $1/10 \text{ sol}^{-1} \leq f \leq 1/1.6 \text{ sol}^{-1}$ range will be smaller than an average taken over, for example, a $1/3.3 \text{ sol}^{-1} \leq f \leq 1/1.6 \text{ sol}^{-1}$ range. Additionally, since the

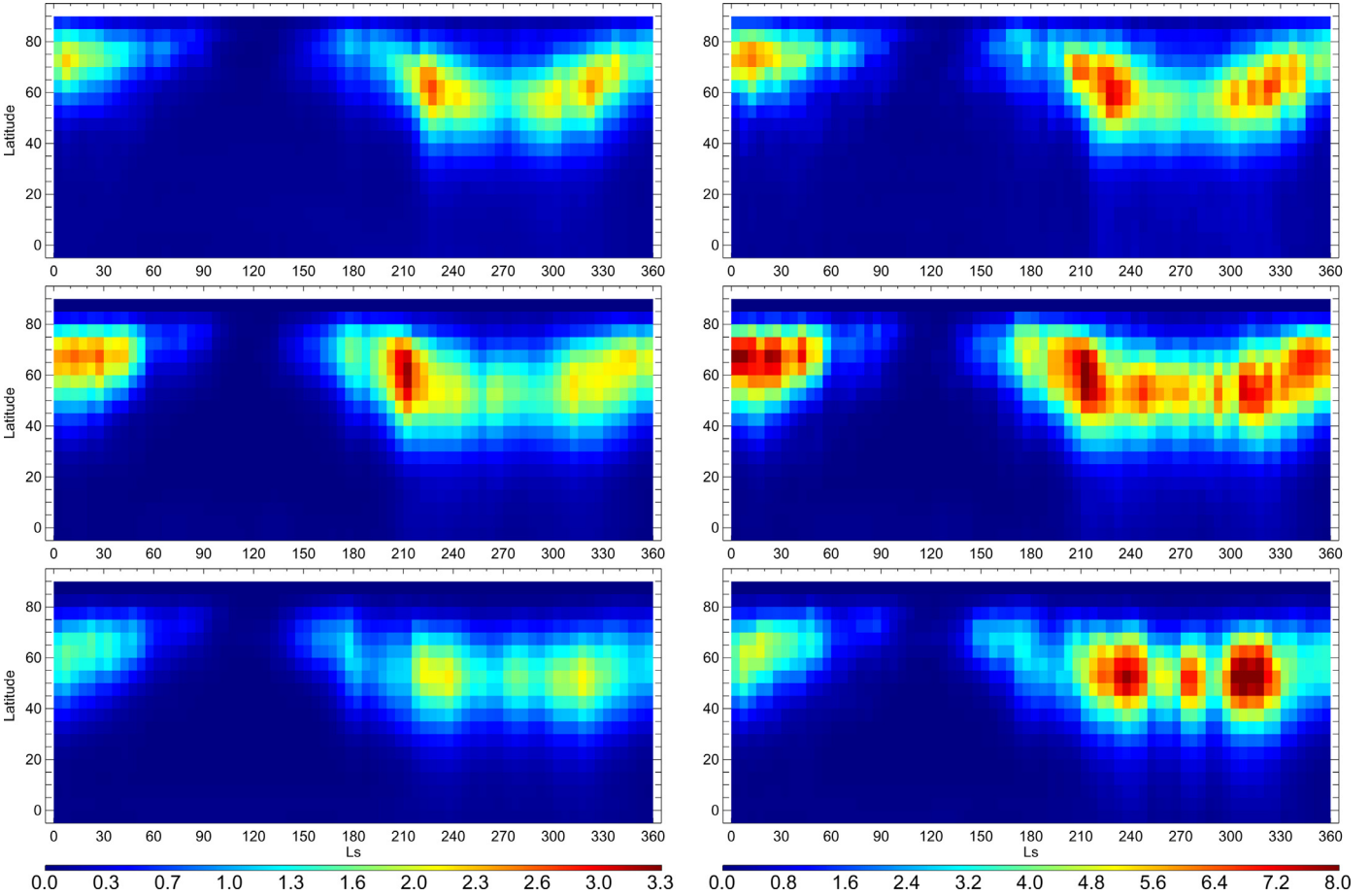


Fig. 2. The L_s versus latitude distributions of the average (left column) and maximum (right column) amplitudes of the zonal wavenumber $m = 1$ (top), $m = 2$ (middle) and $m = 3$ (bottom) eastward traveling waves in the temperature field (in K) at $\eta \sim 0.69$ ($h \sim 4$ km) of “Simulation A”.

seasonal time period when the $m = 3$ waves are most active is inter-annually variable (Fig. 1), if a strong $m = 3$ wave occurred in a particular L_s bin only once during 9 years, the time average would de-emphasize that period of activity.

To account for the possible bias introduced by spectral and temporal averaging, we also analyze the maximum amplitude of the $1.6 \leq P \leq 10$ sols traveling waves in the right column of Fig. 2. For each zonal wavenumber and latitude, the peak amplitude is first found in the wave frequency space corresponding to the $1.6 \leq P \leq 10$ sols wave period range. Then, in a procedure similar to the averaging method described above, those peak amplitudes are binned by solar longitude in $5^\circ L_s$ bins. Finally, the maximum of each solar longitude bin is recorded.

Fig. 2 shows both the average (left column) and the maximum (right column) amplitudes for “Simulation A” as derived from the procedures above. The three rows correspond to zonal wavenumber $m = 1, 2$ and 3 eastward traveling waves, respectively. For ease of comparison with Wang et al. (2013), results are shown for the temperature field at $\eta \sim 0.69$ (~ 4 km high). In agreement with the observations (Lewis et al., 2016; Kavulich et al., 2013; Wang et al., 2013), the model simulates apparent $m = 1\text{--}3$ traveling waves in the northern mid/high latitudes from the fall to the early spring. Moreover, in each panel, the amplitude of the northern mid/high latitude traveling waves near the northern winter solstice ($L_s = 270^\circ$) is generally a local minimum during the fall-winter-spring period. The one exception is the lower right panel where, in one particular year, the simulated $m = 3$ traveling waves reach a peak amplitude of ~ 6 K, whereas in the other 8 years, the

amplitudes of the $m = 3$ waves are much smaller. This rare occasion suggests that inter-annual variability should be taken into account in studies of traveling waves.

Fig. 2 highlights the fact that conclusions about the relative strength of the $m = 1\text{--}3$ waves depends on the analysis method. That is, when considering the average amplitudes (left column), the $m = 3$ waves are generally weaker than the $m = 1$ and $m = 2$ waves (broadly across the times and places of significant wave activity in all wave modes). However, when considering the maximum amplitudes (right column), the $m = 3$ waves are often stronger than the $m = 1$ waves, and are comparable to and sometimes stronger than the $m = 2$ waves at similar seasons and latitudes. Examining an L_s versus latitude plot of the spectral peaks of the $m = 1\text{--}3$ traveling waves for each model year (not shown), we find that the maximum amplitude of the $m = 3$ waves across the northern mid/high latitudes is larger than that of the $m = 1$ and $m = 2$ waves in 3 out of 9 years.

In Fig. 3, we analyze the traveling waves in the temperature field at $\eta \sim 0.91$ ($h \sim 1$ km, left column) and $\eta \sim 0.047$ ($h \sim 33$ km, right column) in “Simulation A”. The heights of these two MarsWRF η levels are the closest to the two MACDA σ levels used in Fig. 1. We use the same analysis method as that used to generate Fig. 1. Fig. 3 shows the largest amplitude of the dominant $m = 1, 2$ and 3 wave modes within the $1.6 < P \leq 15$ sols wave period range and the $0^\circ\text{--}90^\circ\text{N}$ latitude range as a function of L_s for representative years. At $\eta \sim 0.047$, the amplitudes of the $m = 1$ traveling waves far exceed those of the $m = 2$ and $m = 3$ traveling waves from mid-fall to mid-winter. Near the surface ($\eta \sim 0.91$), the

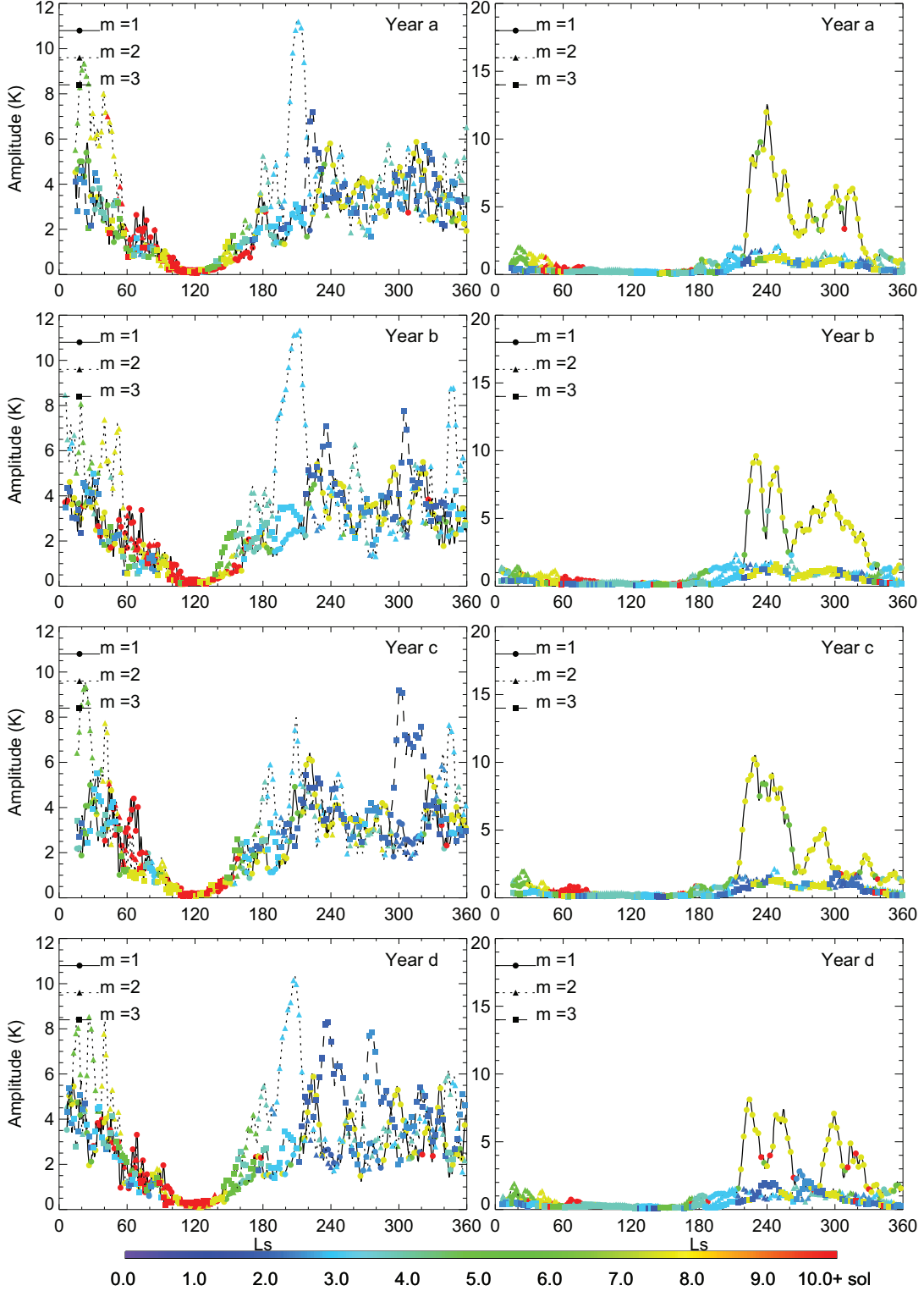


Fig. 3. The maximum amplitude of the northern hemisphere $m = 1$ (solid line with dot), $m = 2$ (dotted line with triangle) and $m = 3$ (dashed line with square) eastward traveling waves as a function of L_s for four representative years of “Simulation A” (Year a, b, c and d). Results are derived from the temperature field (in K) at $\eta \sim 0.91$ ($h \sim 1$ km, left column) and $\eta \sim 0.047$ ($h \sim 33$ km, right column), respectively. The plotting procedure is the same as that used in Fig. 1.

$m = 3$ traveling waves ($P = 2\text{--}3$ sols) can compete with the $m = 1$ ($P = 7.5$ sols) and $m = 2$ ($P = 3\text{--}4$ sols) traveling waves for various L_s periods. For example, there is a wave mode transition that goes from an $m = 2$ to $m = 3$ to $m = 1$ to $m = 2$ during $L_s 200^\circ\text{--}250^\circ$ in Year a.

This wave mode transition can also be seen in eddy kinetic energy. Fig. 4 shows the domain-averaged eddy kinetic energy of the dominant wave mode for zonal wavenumber $m = 1\text{--}3$ as a function of time. At each time step, we calculate the average of the eddy kinetic energy weighted by mass ($\langle E \rangle = \iint Edpd\varphi / \iint dpd\varphi$) for the

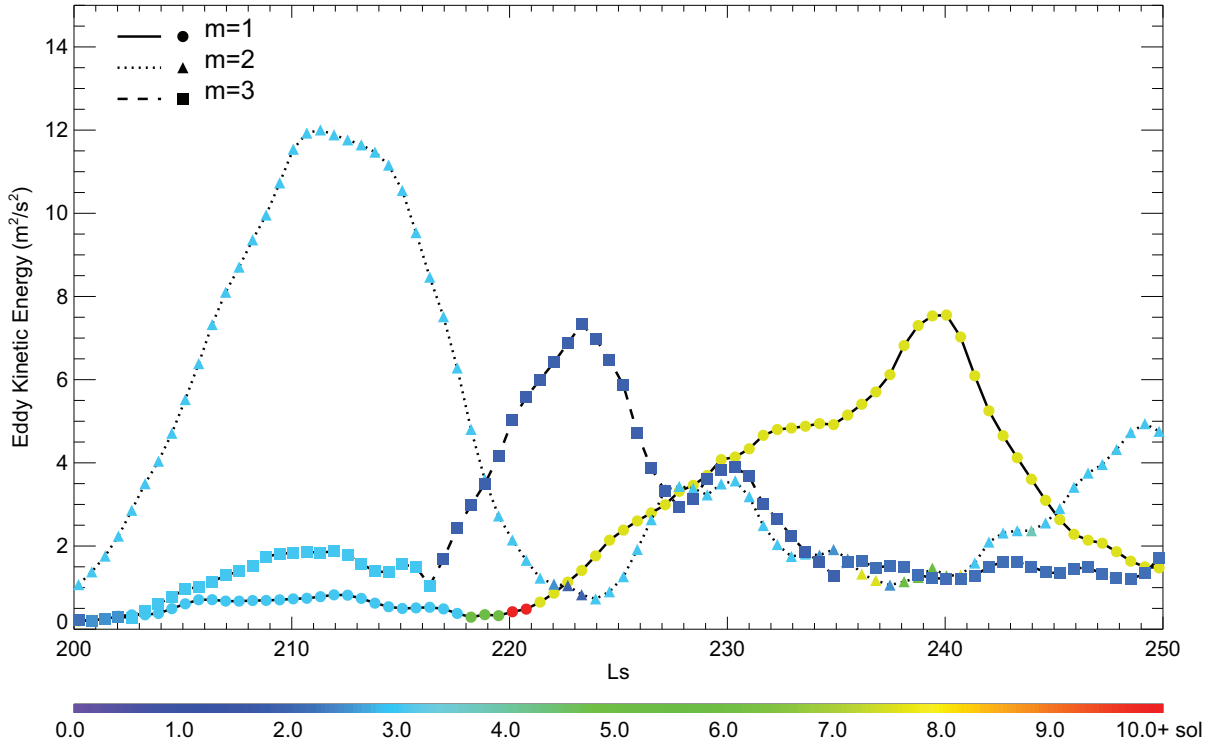


Fig. 4. Time series of the domain-averaged eddy kinetic energy for the dominant $m=1$ (solid), $m=2$ (dotted) and $m=3$ (dashed) eastward traveling waves. The symbol colors indicate the wave periods for the corresponding wave modes.

domain from $\varphi = 0^\circ$ to $\varphi = 90^\circ$ N and from $p(\eta = 1)$ to $p(\eta = 0.069)$ (corresponding to the lowest ~ 50 km of the atmosphere). The eddy kinetic energy E for each wave mode at each latitude φ and level η is calculated using the u and v wind components' wave amplitudes that are derived using the same method as that for Fig. 3. Clearly, the dominant wave mode changes from an $m=2$ to $m=3$ to $m=1$ to $m=2$ during $L_s = 200\text{--}250^\circ$ in Year a.

Due to the differences in dust loading and the differences in model structure and physics parameterizations between MarsWRF and MACDA, the MarsWRF results (Figs. 3 and 4) are not expected to exactly reproduce the MACDA wave mode transitions (Fig. 1). Nevertheless, the qualitative behaviors of the simulated traveling waves appear similar in terms of the general wave mode transitions among zonal wavenumbers $m=1\text{--}3$ near the surface, the corresponding wave periods near the surface, and the dominance of the $m=1$ waves at higher altitudes.

5. Wave structure

We investigate the wave structure in the temperature (Fig. 5) and geopotential (ϕ) fields (Fig. 6) for representative wave modes of the $m=1, 2$ and 3 traveling waves. The eddy fields are extracted on model η levels and plotted using the height estimated from a scale height of 10.8 km. For each wave mode, we plot at a time when the corresponding wave mode dominates the wave spectra near the surface (Fig. 3). Specifically, we plot the $m=1$, $P=6.5$ sols eastward traveling wave at $L_s = 234.5^\circ$ in Year a, the $m=2$, $P=3.0$ sols eastward traveling wave at $L_s = 212.2^\circ$ in Year a, and the $m=3$, $P=2.0$ sols eastward traveling wave at $L_s = 224.9^\circ$ in Year a. To better resolve each wave mode, we use a 13-sol analysis window for the $m=1$ wave, a 12-sol window for the $m=2$ wave and a 10-sol window for the $m=3$ wave. With these choices, an integer number of wave periods can fit into each window. The vertical cross sections (left columns of Figs. 5 and 6) are plotted at 52.5° N which is at or near the latitude of wave amplitude maximum (Fig. 2). The

horizontal cross sections (middle and right columns of Figs. 5 and 6) are shown for a representative lower altitude ($\eta \sim 0.69$, $h \sim 4$ km, middle column) and a representative higher altitude ($\eta \sim 0.047$, $h \sim 33$ km, right column). The pattern shown in each panel is at a single instant in time from the model output. It should be considered to propagate eastward with time at a phase speed of $\sim 55^\circ/\text{sol}$ for the $m=1$ wave, $60^\circ/\text{sol}$ for the $m=2$ wave, and $60^\circ/\text{sol}$ for the $m=3$ wave.

The left column of Fig. 5 shows that the temperature signatures of the $P=3.0$ sols $m=2$ and the $P=2.0$ sols $m=3$ waves are concentrated near the surface (within the first scale height or so) and decay rapidly with height, though weak signals are still discernable at about 40 km and above. There is a node in the phase line at about 15 km for the $m=3$ wave. Near the surface, the phase line of the $m=3$ wave in the temperature field tilts eastward with height. The reverse happens at higher altitudes. The phase shift of the $m=3$ wave is consistent with the result in Wang et al. (2013). For the $m=2$ wave, the phase of the 3 K contour shifts westward with respect to the phase of the 9 K contour near the surface, and the phase of the 1 K contour above ~ 20 km suggests an eastward phase tilt with height. The $P=6.5$ sols $m=1$ wave shows its maximum amplitude at about 35 km, and a weaker secondary maximum near the surface. The phase line of the $m=1$ wave shifts westward with height below ~ 50 km. This wave resembles the $P=6.5$ sols $m=1$ eastward traveling wave simulated in the GFDL Mars GCM by Wilson et al. (2002). The contrasting temperature structure between the $m=1$ wave and the other two waves is in general agreement with the results derived from the MGS TES data (Banfield et al., 2004).

The middle column of Fig. 5 shows the horizontal temperature structures of the waves near the surface ($\eta \sim 0.69$, $h \sim 4$ km). All three wave modes show eastward phase shift with increasing latitude. The right column of Fig. 5 shows the horizontal temperature structures at a higher altitude ($\eta \sim 0.047$, $h \sim 33$ km). Compared with the near surface results, the wave amplitude for the

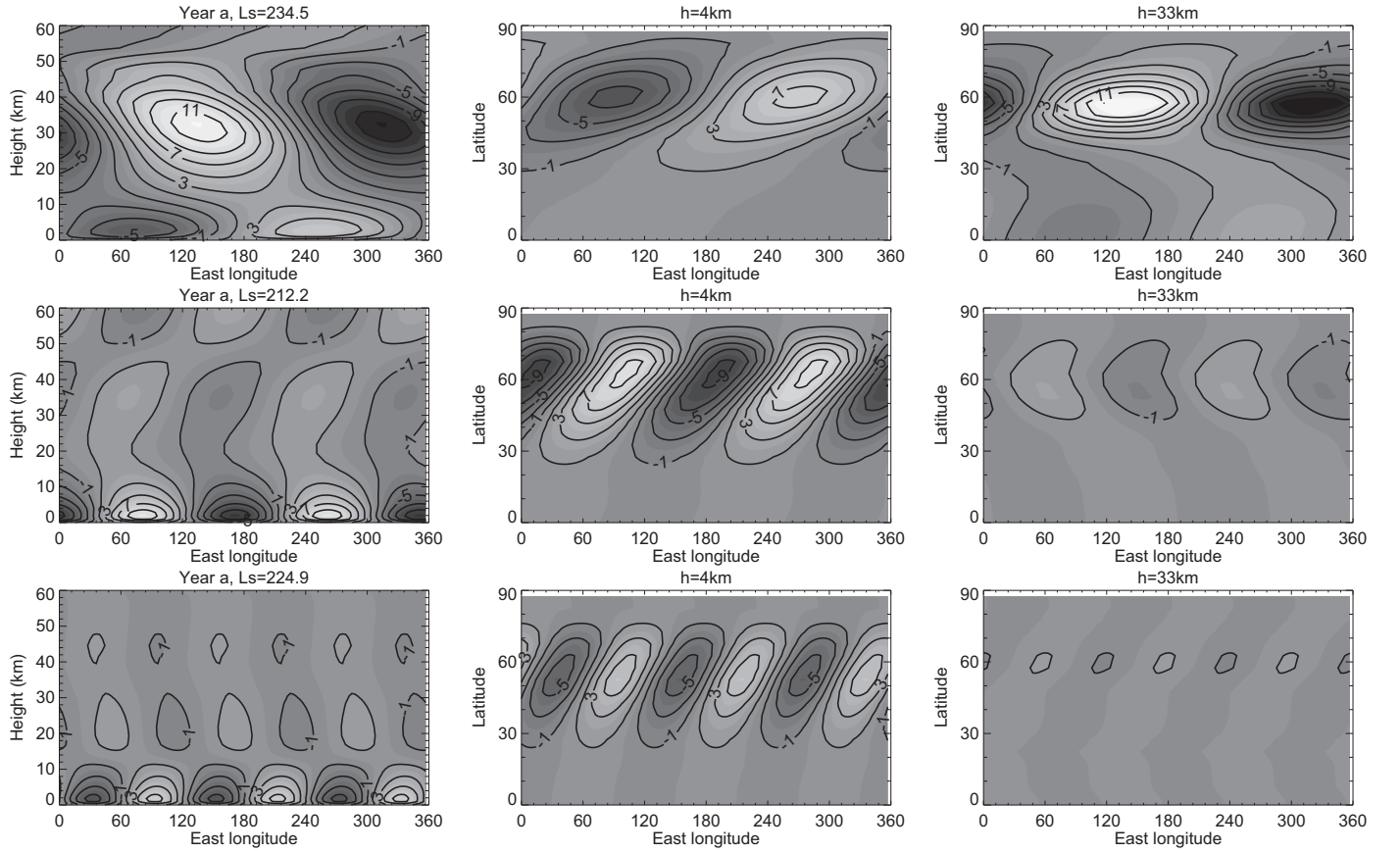


Fig. 5. The eddy temperature (in K) distributions for the $P=6.5$ sols $m=1$ (top), $P=3$ sols $m=2$ (middle) and $P=2$ sols $m=3$ (bottom) eastward traveling waves in “Simulation A”. The eddy fields are extracted on model η levels and plotted using estimated heights. The left column shows the vertical cross section at 52.5°N . The other two columns show the horizontal cross sections at $\eta \sim 0.69$ ($h \sim 4\text{ km}$, middle) and $\eta \sim 0.047$ ($h \sim 33\text{ km}$, right). The $m=1$ mode is plotted for $L_s = 234.5^\circ$, the $m=2$ mode for $L_s = 212.2^\circ$, and the $m=3$ mode for $L_s = 224.9^\circ$ (all in Year a).

$P=6.5$ sols $m=1$ wave is apparently larger than those of the $P=3.0$ sols $m=2$ and $P=2.0$ sols $m=3$ waves. At this upper level, the $m=3$ wave still shows an eastward phase shift with increasing latitude in the mid and high latitudes. But the phase line of the $m=2$ wave tilts eastward with increasing latitude north of $\sim 60^\circ\text{N}$ and westward with increasing latitude south of it. The amplitude of the $m=1$ wave maximizes at $\sim 60^\circ\text{N}$ and the eddy appears to have less tilt than nearer the surface. The $m=1$ wave at $\eta \sim 0.047$ also appears to have a secondary maximum in the low latitudes. Although very weak, it suggests an extension of the wave into the tropics at higher altitudes (Wilson et al., 2002; Banfield et al., 2004). Comparing the horizontal structures in Fig. 5 with those derived at other time steps for the same wave modes, we find that the upper-level structures are sometimes quite different, but the lower level structures are generally the same as those in Fig. 5.

Fig. 6 shows the corresponding wave structures in the geopotential field (ϕ) for the three waves shown in Fig. 5. Although geopotential and temperature can be related through the hydrostatic equation, the patterns in the geopotential field are different than those in the temperature field. This is consistent with Barnes et al. (1993) who showed large differences among various eddy fields simulated by the NASA Ames GCM. The left column of Fig. 6 shows that the eddy geopotential maximum is located at higher altitudes than the equivalent eddy temperature maximum in Fig. 5. This is particularly helpful for the $m=3$ wave since its shallow temperature signature near the surface is challenging to observe with high vertical resolution using TES-like instruments from space (Hinson et al., 2004). Geopotential and winds derived from radio occultation measurements can be used to complement

temperature observations (Hinson and Wang, 2010). Since not every sounding extends down to the surface, there are usually more plentiful radio occultation data at higher altitudes. When data coverage is sparse near the surface but abundant above, analysis of the geopotential at higher altitudes could be used to identify the $m=3$ traveling wave. For the $m=1$ and $m=2$ waves, the phase lines tilt westward with height below the geopotential maximum. For the $m=3$ wave, the phase lines tilt westward with height above $\sim 15\text{ km}$ and slightly eastward below that. Westward phase tilt with height for geopotential is a signature of baroclinic waves (e.g., Holton and Hakim, 2013). The middle and right columns of Fig. 6 show the longitude versus latitude structures of the eddy geopotential at the same η levels as the corresponding columns in Fig. 5. For all three waves, the amplitudes maximize within $50^\circ\text{N}-60^\circ\text{N}$, and the phase lines tilt eastward with increasing latitude around the amplitude maxima. For the $P=6.5$ sols $m=1$ wave, there is an indication that the wave amplitude has a very weak secondary maximum in the low latitudes, and the corresponding phase line exhibits little tilt with latitude. Again, the upper-level patterns are sometimes different at other time steps than those shown in Fig. 6.

6. Energy conversion analysis

6.1. Representative wave modes

Wang et al. (2013) investigated several components of the energy cycle of band pass filtered transient eddies using the Ulbrich and Speth (1991) formulation. They found that, near the surface, the eastward propagating $1.4 \leq P \leq 10$ sol $m=3$ waves mainly

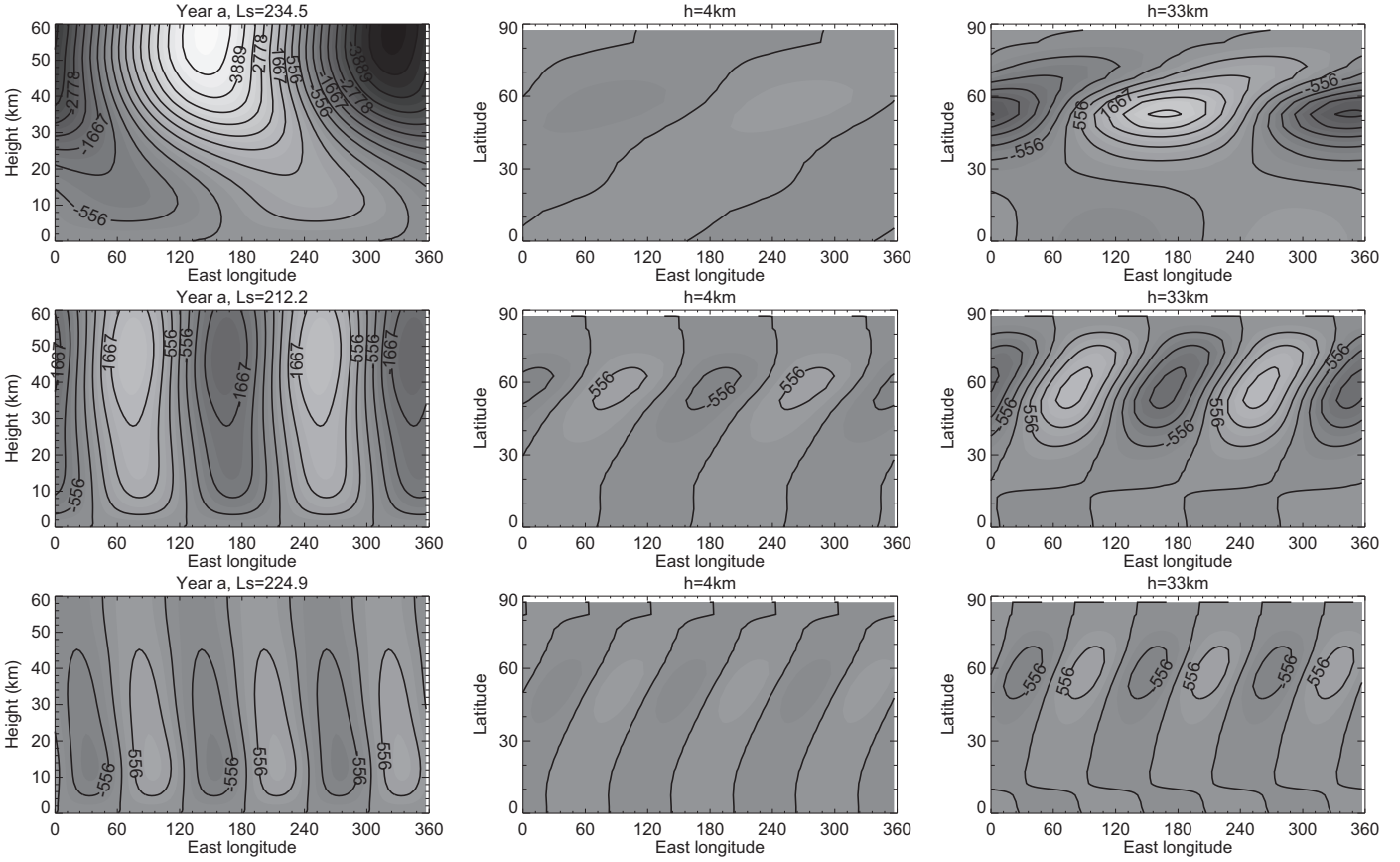


Fig. 6. The same as Fig. 5, but for the eddy geopotential field (in m^2/s^2).

generated their kinetic energy through baroclinic energy conversion from eddy available potential energy, and decayed through the transfer of eddy kinetic energy to the zonal mean flow.

In this paper, we investigate selected components of the energy cycle for the wave modes shown in Fig. 5 using the Hayashi and Golder (1983) method. Their formulation expresses the energy equation as the following:

$$\frac{\partial K_n}{\partial t} = \langle K_0 \cdot K_n \rangle + \langle K_m \cdot K_n \rangle - C_n(\alpha, \omega) - \left[\frac{\partial C_n(\phi, v)}{\partial y} + \frac{\partial C_n(\phi, \omega)}{\partial p} \right] + [C_n(u, F_u) + C_n(v, F_v)] \quad (2)$$

where, n and m are wave modes (i.e., each wave mode is a representation of a single wavenumber and a single wave period). The subscript 0 denotes the wave modes associated with zonal wavenumber 0 (which is a zonal mean, but not a time mean). K_n is the eddy kinetic energy of wave mode n . $\langle K_0 \cdot K_n \rangle$ represents the transfer of kinetic energy to wave mode n by the interaction between the zonal flow and wave mode n . $\langle K_m \cdot K_n \rangle$ represents the transfer of kinetic energy to wave mode n by the interactions among all the wave modes represented by m , i.e., wave-wave interaction. $C_n(x, y)$ denotes the co-spectrum between variable x and variable y . The term $-C_n(\alpha, \omega)$ represents baroclinic energy conversion from eddy available potential energy to eddy kinetic energy. The term $-\left[\frac{\partial C_n(\phi, v)}{\partial y} + \frac{\partial C_n(\phi, \omega)}{\partial p} \right]$ represents the effect of geopotential convergence. It contributes strongly to the local energy budget, but vanishes when integrated globally. The term $[C_n(u, F_u) + C_n(v, F_v)]$ represents dissipation by friction, and is usually diagnosed from other terms. Errors tend to accumulate in this term. In addition, as will be defined below, our domain of interest is mostly above the surface which is a major source of

friction. Therefore, we do not investigate the dissipation term any further in this paper.

To apply Eq. (2), we interpolate the model output to 15 (unevenly spaced) pressure levels between 610 Pa and 6 Pa (between about 0–50 km above the 610 Pa reference level, at about 2–5 km intervals). We first interpolate in the vertical, from the model η levels to the pre-selected pressure levels, assigning a missing value to the pressure levels that are below the ground at that location and time. For the pressure levels containing missing values, if the number of missing grid points is less than 50%, we further interpolate horizontally to fill in the gaps. Many methods can be used to estimate the space-time spectra (Hayashi, 1982). The Fourier transform method is used here due to its computational efficiency. As in the previous section, we use a 13-sol (for the $m=1$ wave), 12-sol (for the $m=2$ wave) or 10-sol (for the $m=3$ wave) window that encompasses the instant in time shown in Fig. 5. Note that the effects of eddies with wave periods longer than the window lengths are excluded in this analysis.

We investigate the latitude versus height distributions of the baroclinic, barotropic, geopotential convergence and wave-wave interaction terms in the northern hemisphere in Fig. 7. Different columns correspond to the $P=6.5$ sols $m=1$ (left), $P=3.0$ sols $m=2$ (middle) and $P=2.0$ sols $m=3$ (right) eastward traveling waves. The heights on the left axis are estimated from the pressures on the right axis, assuming a 10.8 km atmospheric scale height and a 610 Pa reference surface at 0 km. The results are derived around the times equivalent to those used for Fig. 5.

The first row shows the baroclinic term $-C_n(\alpha, \omega)$. Positive values indicate energy conversion from eddy potential energy (PE, superimposed contours) to eddy kinetic energy (KE) through warm air rising/cold air sinking. The eddy PE for the $m=2$ and $m=3$

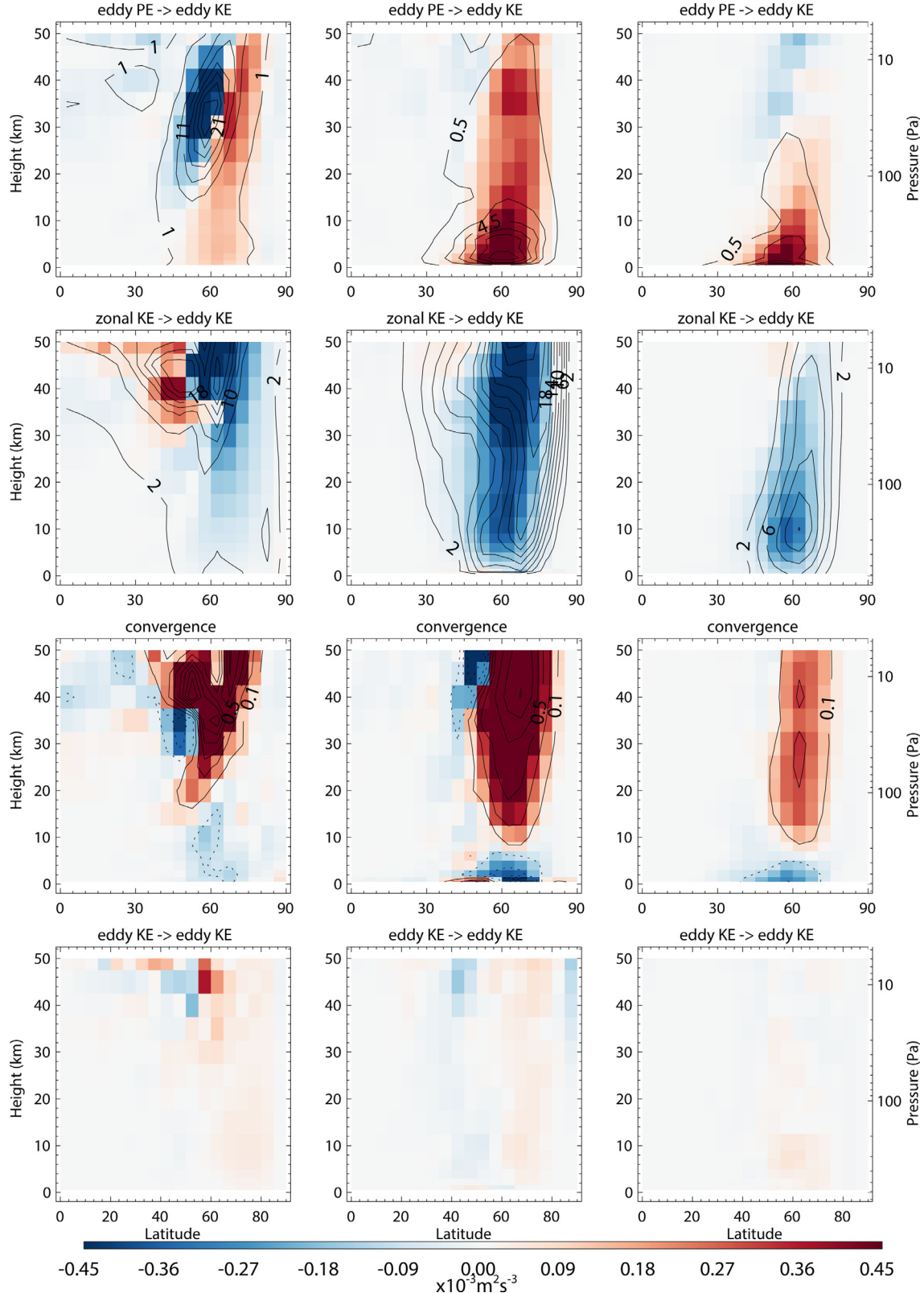


Fig. 7. Latitude versus height cross sections of various eddy energetics components for the $P = 6.5$ sol $m = 1$ (left), $P = 3$ sol $m = 2$ (middle) and $P = 2$ sol $m = 3$ (right) eastward traveling waves. Height is estimated from pressure (on the right-hand) using a scale height of 10.8 km and a reference pressure of 610 Pa. The first row shows the conversion rates from eddy potential energy to eddy kinetic energy. The second row shows the conversion rates from zonal kinetic energy to eddy kinetic energy. The third row shows the geopotential flux convergences. Contours for this term ($\text{m}^2 \text{ s}^{-3}$) are over-plotted to better represent the range of values. The fourth row shows the conversion rates due to wave-wave interactions. The superimposed contours in the first row show the corresponding eddy potential energy ($\text{m}^2 \text{ s}^{-2}$). For $m = 1$, the contours start at $1 \text{ m}^2 \text{ s}^{-2}$ and are spaced at $5 \text{ m}^2 \text{ s}^{-2}$. For $m = 2$ and $m = 3$, the contours start at $0.5 \text{ m}^2 \text{ s}^{-2}$ and are spaced at $2 \text{ m}^2 \text{ s}^{-2}$. The superimposed contours in the second row show the corresponding eddy kinetic energy ($\text{m}^2 \text{ s}^{-2}$). For $m = 1$, the contours start at $2 \text{ m}^2 \text{ s}^{-2}$ and are spaced at $4 \text{ m}^2 \text{ s}^{-2}$. For $m = 2$ and $m = 3$, the contours start at $2 \text{ m}^2 \text{ s}^{-2}$ and are spaced at $2 \text{ m}^2 \text{ s}^{-2}$.

waves maximizes near the surface, but that for the $m=1$ wave maximizes near ~ 35 km. All three wave modes gain eddy KE through baroclinic processes near the surface. However, at upper levels, there are negative baroclinic conversion regions on the equatorward side of the positive conversion regions. This is especially apparent for the $m=1$ wave and discernable for the $m=3$ wave. In agreement with this result, Wang et al. (2013) also found a negative baroclinic conversion region at upper levels for the $1.4 \leq P \leq 10$ sols eastward traveling $m=3$ waves in their Fig. 12. Although the negative region for the $m=2$ wave at upper levels is only slightly negative in Fig. 7, it can achieve larger negative amplitudes at other times (not shown).

The second row of Fig. 7 shows the $\langle K_0 \cdot K_n \rangle$ term which can be considered as the barotropic energy conversion between the wave and zonal flow. Positive values indicate kinetic energy conversion from the zonal flow to the eddy. The eddy KE (superimposed contours) for the $m=1$ wave maximizes above ~ 45 km and extends to both the low latitudes and the high latitudes at upper levels. The eddy KE for the $m=3$ wave maximizes at about 10 km. The contours for the $m=3$ eddy KE tilt poleward with height and are confined within the mid/high latitudes. The pattern of the eddy KE for the $m=2$ wave appears to be a combination of the other two wave modes. The $m=1$ wave apparently switches from positive to negative $\langle K_0 \cdot K_n \rangle$ conversion rate around 50°N at upper levels. It gains kinetic energy from the zonal flow equatorward of $\sim 50^{\circ}\text{N}$ and loses kinetic energy to the zonal flow poleward of it. The $m=2$ and $m=3$ waves lose their kinetic energy to the zonal flow throughout most of the regions where eddy KE is significant, though there are indications of positive conversion regions equatorward of the negative ones at upper levels. The existence of a positive $\langle K_0 \cdot K_n \rangle$ region is consistent with Barnes et al. (1993) who found that barotropic energy conversion could be a source of eddy KE at upper levels in their simulations. Fig. 7 suggests that barotropic energy conversion is mainly a sink for the waves, but can be a source in the low to mid latitudes at upper levels, especially for the $m=1$ wave above ~ 20 km.

The third row of Fig. 7 shows the geopotential flux convergence. Positive values act as local sources of eddy KE. Although the global integral of this term vanishes, it can be a major contributor locally. Generally speaking, for the $m=1$ and $m=2$ waves, convergence is seen at upper levels, divergence is seen near the surface and equatorward of the upper level convergence. For the $m=3$ wave, near the surface, this term reduces eddy KE along with the barotropic term, but above ~ 5 km, this term supplies eddy KE which is dissipated by barotropic and baroclinic processes.

The fourth row of Fig. 7 shows the contribution of wave – wave interaction. This term is generally much smaller than the other terms, but can be significant sometimes (e.g., at upper levels for the $m=1$ wave). The pattern and magnitude of this term are highly variable with time. This wave – wave interaction could probably influence the variability of traveling waves and will be discussed a little further in the next section.

6.2. Band-pass filtered Eddies

Kavulich et al. (2013) found large zonal variations in eddy amplitudes and energy conversion terms for band-pass filtered eddies simulated in the GFDL Mars GCM. To examine the spatial distributions of various eddy energetics components in our simulation, we apply the Sheng and Derome (1991) frequency domain analysis method for band-pass filtered transient eddies. In this method, the meteorological fields are decomposed into the time mean flow (including stationary waves and the time and zonal mean) and transient eddies. The transient eddies are further decomposed into a low frequency and a high frequency band (regardless of zonal wavenumber). As a result, the interaction of each frequency

band with the time mean flow can be studied, and the interaction between the two frequency bands can be diagnosed. Sheng and Derome (1991) used the following terms to describe the transfer of eddy kinetic energy for each frequency band: LK represents the transfer of kinetic energy from the time-mean flow to transient eddies (which we call “the barotropic term”), AK represents the energy conversion from eddy available potential energy to eddy kinetic energy (which we call “the baroclinic term”), NK represents the transfer of kinetic energy due to nonlinear interactions between the high-frequency and low-frequency transient eddies (which we call “the nonlinear wave interaction term”), FK represents the convergence of transient eddy kinetic energy, FP represents the convergence of transient flux of geopotential, and D represents the dissipation. As in the previous section, we do not specifically diagnose D in this paper.

In Fig. 8, we decompose the transient eddies into a high-frequency band of $P < 1.6$ sols and a low-frequency band of $1.6 \leq P \leq 15$ sols for each 15-sol time window. The three columns correspond to three different 15-sol time windows. The eddy KE for the high-frequency band is dominated by thermal tides, and that for the low-frequency band is dominated by $m=1\text{--}3$ eastward traveling waves (not shown). We calculate the mass-weighted average of each term ($\bar{X} = \int X dp / \int dp$) over the $p = 6 \text{ Pa} \text{--} 610 \text{ Pa}$ range at each location. The AK (top row), LK (middle row), and FP (not shown) terms are much stronger than the NK (bottom row) and FK (not shown) terms, and the NK term is usually stronger than the FK term.

In the middle column of Fig. 8, we focus on a 15-sol time window when the $P=2$ sols $m=3$ wave is dominant ($L_s = 217.9^{\circ}\text{--}227.4^{\circ}$ in Year a, Fig. 4). The eddy KE of the $1.6 \leq P \leq 15$ sols eddies shows three local maxima in the northern mid-latitudes, near -10°E , 120°E and -175°E , respectively. These locations correspond to the low topography regions of Acidalia, Utopia, and Arcadia Planitias. This spatial pattern correlates well with the routes of flushing dust storms observed in images (Wang et al., 2013; Wang and Richardson, 2015). Using the NASA Ames GCM, Hollingsworth et al. (1996) also found three local eddy KE maxima in these locations and referred to them as the martian “storm zones”. They found that the locations of these storm zones were controlled by planetary-scale orography.

The middle column of Fig. 8 also shows apparent zonal variations in the energetics terms. Positive/negative values indicate that eddies are gaining/losing KE. The Acidalia eddy KE center is located to the east (downstream) of the strongest AK center where baroclinic processes convert eddy PE to eddy KE. It is almost collocated with or slightly upstream of the strongest negative LK center where eddy KE is lost to the time mean flow. The FP term (not shown) exhibits a positive region upstream and a negative region downstream of this eddy KE center. The Utopia eddy KE center has larger amplitude than the Acidalia KE center. It is also downstream of the corresponding AK center and associated with a positive-negative dipole pattern in FP . However, it does not seem to be associated with a local negative LK center. The Arcadia eddy KE center appears to be west (upstream) of the corresponding AK and LK extrema and associated with a negative-positive dipole pattern in FP . The non-linear influence of the high-frequency ($P < 1.6$ sols) eddies on the low-frequency ($1.6 \leq P \leq 15$ sols) eddies exhibits banded spatial patterns near the eddy KE centers. This wave – wave interaction is much weaker than the other terms shown. Consequently, the $1.6 \leq P \leq 15$ sols eddies are mainly interacting with the time mean flow through baroclinic and barotropic processes, though non-linear wave-wave interaction is also occurring. This reinforces the inference drawn in Kavulich et al. (2013) that the energy exchange between the transient eddies and thermal tides was weak compared with the energy exchange between the transient eddies and the mean flow.

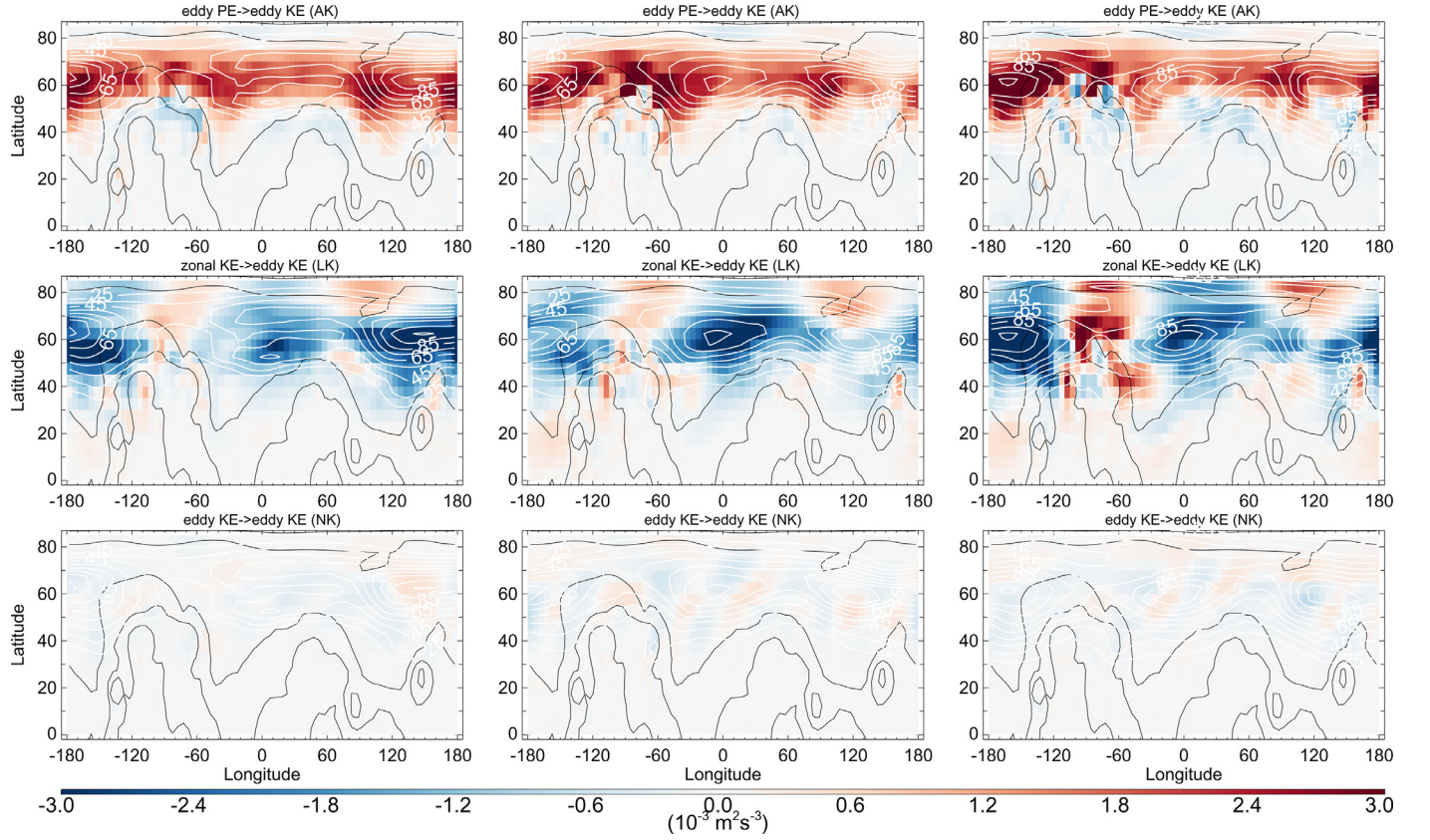


Fig. 8. Maps of the mass-weighted average of eddy kinetic energy (white contours, in $\text{m}^2 \text{s}^{-2}$) and energy conversion terms (colors, in $10^{-3} \text{ m}^2 \text{s}^{-3}$) for the $1.6 \leq P \leq 15$ sols transient eddies. The black contours indicate topography. The top row shows the conversion rates from eddy potential energy to eddy kinetic energy (AK). The middle row shows the conversion rates from time mean kinetic energy to eddy kinetic energy (LK). The bottom row shows the transfer of kinetic energy from the $P < 1.6$ sols eddies to the $1.6 \leq P \leq 15$ sols eddies (NK). The left column is for $L_s = 210.4^\circ\text{--}219.8^\circ$, the middle column is for $L_s = 217.9^\circ\text{--}227.4^\circ$, and the right column is for $L_s = 225.5^\circ\text{--}235.1^\circ$, all in Year a.

In Fig. 8, we also examine two other 15-sol time windows that are adjacent to the one discussed above. The time window in the left column corresponds to $L_s = 210.4^\circ\text{--}219.8^\circ$ in Year a. During this time period, there is a wave mode transition from $m = 2$ to $m = 3$, but the $m = 2$ wave is overall stronger (Fig. 4). We find two local maxima in eddy KE – one in Acidalia and the other connecting Utopia and Arcadia. The spatial patterns of the energy conversion terms shift accordingly. Again, the nonlinear interaction term is much smaller than the other two. However, in comparison to the bottom middle panel, the spatial pattern shows less frequent zonal variation, which is probably related to the longer wavelength of the $m = 2$ wave. Using the GFDL Mars GCM, Kavulich et al. (2013) also found two eddy KE maxima near Acidalia and Utopia in their simulation which was dominated by an $m = 2$ traveling wave at the time.

The right column of Fig. 8 is for the time window $L_s = 225.5^\circ\text{--}235.1^\circ$ in Year a. During this time period, the $m = 3$ wave is weakening, the $m = 1$ wave is strengthening, and the $m = 2$ wave is first strengthening then weakening (Fig. 4). The positions of the local extrema of the energetics terms are similar to those shown in the middle column of Fig. 8, but the relative strength of the AK, LK and eddy KE centers apparently shifts in favor of Arcadia. While most flushing dust storms were observed in the Acidalia channel, some were observed in the Utopia and Arcadia channels (Wang and Richardson, 2015). In particular, an impressive Arcadia flushing event was observed during $L_s = 226^\circ\text{--}230^\circ$ in Mars year 24 (Wang and Richardson, 2015). It is interesting that it occurred during a time period when the dominant wave mode was changing from an $m = 3$ to an $m = 2$ (Fig. 1).

In Fig. 9, we further examine the time period of $L_s = 225.5^\circ\text{--}235.1^\circ$ in Year a. Instead of focusing on the interaction between the thermal tides and traveling waves (bottom right panel of Fig. 8), we are now interested in the interactions among the traveling waves. For this purpose, we alter the band-passes used for the high and low frequency bands. Specifically, we calculate the energetics terms using a band-pass of $1.6 \leq P < 5$ sols as the high-frequency band and a band-pass of $5 \leq P \leq 15$ sols as the low-frequency band. The high-frequency band is mainly composed of $m = 2$ and $m = 3$ traveling waves. The low-frequency band is mainly composed of $m = 1$ traveling waves (Fig. 4). Results for the high-frequency band are shown in the left column of Fig. 9. In comparison with the right column of Fig. 8, although the eddy KE, AK and LK conversion rates have smaller amplitudes due to the narrower wave period range, their patterns largely remain the same. However, the nonlinear wave-wave interaction term shows a completely different pattern. Specifically, the $1.6 \leq P < 5$ sols eddies (mainly $m = 2$ and 3) are losing energy to the $5 \leq P \leq 15$ sols eddies (mainly $m = 1$) in a meandering mid-latitude band and are gaining energy in some areas on both sides of the band. This suggests that the detailed mechanism for the interaction between the high and low-frequency traveling waves is different than that between the traveling waves and thermal tides.

We also perform the calculation using a band-pass of $1.6 \leq P < 2.5$ sols as the high-frequency band and a band-pass of $2.5 \leq P \leq 15$ sols as the low-frequency band. The high-frequency band is dominated by $m = 3$ traveling waves. The low-frequency band is composed of $m = 1$ and $m = 2$ traveling waves. Results for the high-frequency band are shown in the right column of Fig. 9. Compared

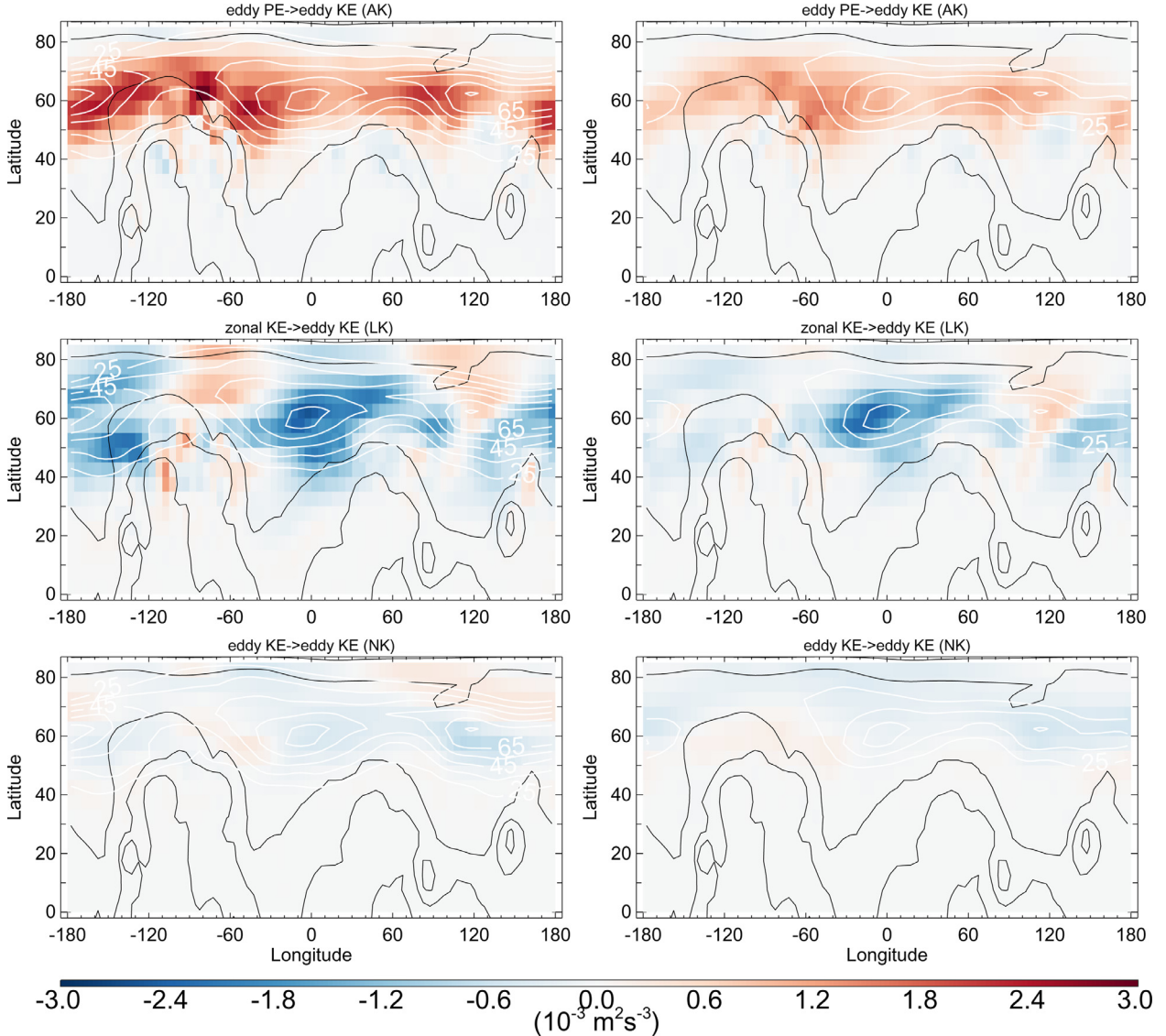


Fig. 9. The same as the right column of Fig. 8, but results are derived from different frequency band partitions. The left column shows the results for the $1.6 \leq P < 5$ sols eddies and their interaction with the $5 \leq P \leq 15$ sols eddies. The right column shows the results of the $1.6 \leq P < 2.5$ sols eddies and their interaction with the $2.5 \leq P \leq 15$ sols eddies.

with the left column of Fig. 9, there are further reductions in the amplitudes of various terms. The nonlinear interaction term shows that the $1.6 \leq P < 2.5$ sols eddies (mainly $m=3$) are losing energy to the $2.5 \leq P \leq 15$ sols eddies north of $\sim 60^\circ$ N. The area with negative value extends to higher latitudes than that in the lower left panel of Fig. 9. Therefore, at these higher latitudes, energy is being transferred from $m=3$ to $m=1$ and $m=2$ traveling waves, and at the same time, energy is being transferred from $m=1$ to $m=2$ and $m=3$ traveling waves.

In Fig. 10, we investigate the temporal evolution of various wave energetics terms for $L_s = 210^\circ\text{--}240^\circ$ in Year a. During this time period, the dominant wave mode transition is from an $m=2$ to $m=3$ to $m=1$ (Fig. 4). First, we perform wave energetics analysis every 3 sols with a 15-sol sliding window using pre-selected high-frequency and low-frequency bands. Then, we calculate the mass weighted averages of the AK, LK, NK and eddy KE terms within the domain of 6 Pa–610 Pa and $0^\circ\text{--}90^\circ$ N for the frequency band of interest for each time window. Finally, we plot their time series.

In the left column of Fig. 10, we use a high-frequency band of $1.6 \leq P < 5$ sols (dominated by $m=2$ and $m=3$ traveling waves) and a low-frequency band of $5 \leq P \leq 15$ sols (dominated by $m=1$ traveling waves) in the calculation. The top left panel shows that the eddy KE generally decreases for the high-frequency band (solid line) and increases for the low-frequency band (dotted line). This is consistent with the evolution of the $m=1\text{--}3$ traveling waves shown in Fig. 4. During $L_s = 220^\circ\text{--}232^\circ$, the $5 \leq P \leq 15$ sols eddies rapidly grow. They become stronger than the $1.6 \leq P < 5$ sols eddies after $L_s \sim 230^\circ$. The AK and LK conversion rates for the $1.6 \leq P < 5$ sols eddies are shown in the middle left panel. Their amplitudes decrease as the corresponding eddy KE decreases with time. The non-linear conversion (NK) from the $5 \leq P \leq 15$ sols eddies to the $1.6 \leq P < 5$ sols eddies is shown by the solid line in the bottom left panel. Note that the unit here is an order of magnitude smaller than that for the middle panel. As discussed before, this term is much smaller than the AK and LK terms. However, since the rate of change of eddy KE is also on the order of $10^{-5} \text{ m}^2 \text{ s}^{-3}$ (not shown), the NK term is non-negligible. This panel shows that

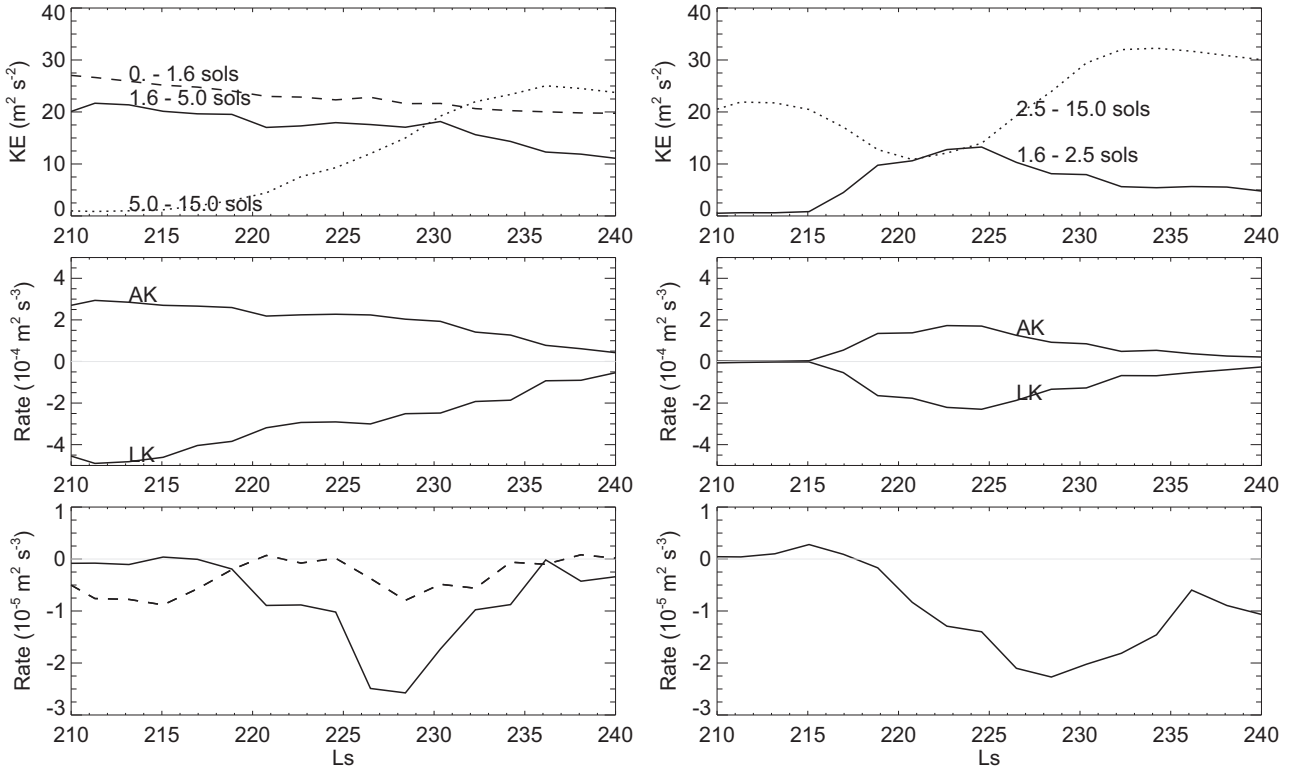


Fig. 10. Time series of eddy KE (top row), energy conversion rates between the transient eddies and the time mean flow (AK and LK, middle row), and nonlinear wave-wave interaction (NK, bottom row) during $L_s = 210^\circ\text{--}240^\circ$ in Year a. The top left panel shows the eddy KE for the $P < 1.6$ sols (dashed line), $1.6 \leq P < 5$ sols (solid line), and $5 \leq P \leq 15$ sols (dotted line) eddies. The top right panel shows the eddy KE for the $1.6 \leq P < 2.5$ sols (solid line) and $2.5 \leq P \leq 15$ sols (dotted line) eddies. The middle left panel shows the AK and LK for the $1.6 \leq P < 5$ sols eddies, and the middle right panel shows those for the $1.6 \leq P < 2.5$ sols eddies. The bottom left panel shows the energy conversion rate from the $5 \leq P \leq 15$ sols eddies to the $1.6 \leq P < 5$ sols eddies (solid line), as well as the energy conversion rate from the $P < 1.6$ sols eddies to the $1.6 \leq P < 5$ sols eddies (dashed line). The bottom right panel shows the energy conversion rate from the $2.5 \leq P \leq 15$ sols eddies to the $1.6 \leq P < 2.5$ sols eddies.

the $1.6 \leq P < 5$ sols eddies are losing energy to the $5 \leq P \leq 15$ sols eddies during $L_s = 220^\circ\text{--}240^\circ$ when the low-frequency eddies are active. In particular, the magnitude of NK maximizes during the $L_s = 225^\circ\text{--}232^\circ$ period which bridges the period dominated by an $m = 3$ wave and the period dominated by an $m = 1$ wave (Fig. 4).

To examine the interaction between the $1.6 \leq P < 5$ sols eddies (dominated by $m = 2$ and $m = 3$ traveling waves) and the $P < 1.6$ sols eddies (dominated by thermal tides) during $L_s = 210^\circ\text{--}240^\circ$ in Year a, we perform calculations using these frequency bands. The eddy KE of the $P < 1.6$ sols eddies monotonically decreases (dashed line in the top left panel). The $1.6 \leq P < 5$ sols eddies lose kinetic energy to the $P < 1.6$ sols eddies during two episodes (dashed line in the bottom left panel). One episode is during $L_s = 225^\circ\text{--}235^\circ$ when eddies are changing from $1.6 \leq P < 5$ sols to $5 \leq P \leq 15$ sols (top left panel). The nonlinear conversion rate is about 1/3 of that represented by the solid line in the same panel. The other episode is during $L_s = 210^\circ\text{--}220^\circ$ when the dominant wave mode is changing from an $m = 2$ to an $m = 3$ traveling wave (Fig. 4). This time, the amplitude of the conversion rate is larger than that represented by the solid line.

In the right column of Fig. 10, we perform an analysis using a high-frequency band of $1.6 \leq P < 2.5$ sols (dominated by $m = 3$ traveling waves) and a low-frequency band of $2.5 \leq P \leq 15$ sols (dominated by $m = 1$ and $m = 2$ traveling waves). The eddy KE of the $1.6 \leq P < 2.5$ sols eddies maximizes when that of the $2.5 \leq P \leq 15$ sols minimizes (top right panel). The interactions of the $1.6 \leq P < 2.5$ sols eddies with the time mean flow (AK and LK) are shown in the middle right panel. Their magnitudes correlate with the corresponding eddy KE. The nonlinear interaction term is shown in the bottom right panel. After $L_s \sim 217^\circ$, the $1.6 \leq P < 2.5$

sols eddies are transferring energy to the $2.5 \leq P \leq 15$ sols eddies. Since the magnitudes are comparable to the solid line in the bottom left panel, the $m = 3$ waves can be inferred to play an important role in the nonlinear interactions among the traveling waves during this time period. Before $L_s \sim 217^\circ$, the NK conversion rate is slightly positive, but its magnitude is significantly smaller than that represented by the dashed line in the lower left panel. For this specific time period, Fig. 10 and other diagnoses (not shown) indicate that the non-linear interactions among the $m = 1, 2$, and 3 traveling waves are generally weaker than the non-linear interactions between the thermal tides and traveling waves. Therefore, our case study period ($L_s = 210^\circ\text{--}240^\circ$) exhibits two general types of non-linear interactions. The early part of this period ($L_s = 210^\circ\text{--}217^\circ$) is mostly the interaction between the thermal tides and traveling waves and the later part ($L_s = 217^\circ\text{--}240^\circ$) is mainly the interaction among the traveling waves.

7. Summary

Traveling waves with zonal wave number 1–3 are prominent in the martian atmosphere. The $m = 3$ traveling waves are closely linked to the martian dust cycle through frontal/flushing dust storms. In this paper, we investigate the variability of traveling waves simulated in the MarsWRF GCM, with a focus on wave mode transitions to and from the $m = 3$ traveling waves. In this context, we analyze the structure and energetics of the major $m = 1\text{--}3$ wave modes involved in the transitions.

Our MarsWRF simulation uses a simple, annually repeatable dust scenario. This scenario has an enhancement of dust at the north polar cap edge relative to the Mars Climate Database “MGS

dust scenario". It allows us to investigate the intrinsic variability due to the dynamics simulated by the model without the complication of inter-annual dust variability. The simulation reasonably reproduces the general characteristics of the observed traveling waves, including the major wave modes, the thermal signatures, the dominance of the $m=1$ waves at high altitudes, the winter solstice hiatus of traveling waves near the surface, and the wave mode transitions.

We have examined the structures of representative wave modes for zonal wavenumbers $m=1-3$ in the eddy temperature and geopotential fields. The temperature signatures of the $m=3$ traveling waves are strongly confined near the surface, and that for the $m=1$ wave maximizes at around 35 km. These are largely consistent with the results derived from the MGS TES observations. The eddy geopotential maxima are generally located at higher altitudes than the corresponding temperature maxima for all three wave modes. This property could probably be exploited for future instruments to better observe the $m=3$ waves.

We find that individual wave modes exhibit both baroclinic and barotropic characteristics. This is consistent with Barnes et al. (1993) who found that the ensemble of transient eddies in their model had a mixed baroclinic-barotropic nature. There is a large contrast in eddy energetics between the lower ($<\sim 20$ km) and higher altitudes ($\sim 20-50$ km) for these wave modes. Near the surface, eddy kinetic energy is supplied by baroclinic conversion from eddy available potential energy (which is generated through conversion from zonal available potential energy) and it is released by barotropic conversion to the zonal flow. At higher altitudes, there is a clear distinction between the lower and higher latitudes (Fig. 7). The higher latitudes are characterized by baroclinic growth and barotropic decay, while the lower latitudes exhibit negative baroclinic and positive barotropic conversion. This indicates that a barotropic energy source is important for the equatorward extension of transient eddies at higher altitudes. Results also suggest that wave-wave interactions are sometimes non-negligible, especially for high altitudes. There are apparent differences in eddy energetics between the $m=3$ and $m=1$ waves. The strongest baroclinic and barotropic energy conversions for the $m=3$ wave mode are located below 20 km, while those for the $m=1$ wave mode are above 20 km.

We have also performed wave energetics analysis for band-pass filtered transient eddies using a method that can diagnose nonlinear wave interactions. We have investigated a time period when the simulated wave modes show a transition from an $m=2$ to $m=3$ to $m=1$ dominant wave mode. Apparent zonal variations are found in the eddy kinetic energy and energy conversion terms. In particular, when a $P=2$ sols $m=3$ eastward traveling wave is active, the eddy kinetic energy exhibits three maxima located near Acidalia, Utopia and Arcadia, respectively. These regions correlate well with the locations of frontal/flushing dust storms which are often involved in the development of major dust storms. The extrema of the energy fluxes are slightly offset from or co-located with the centers of eddy kinetic energy. Nonlinear wave-wave interactions are much weaker than the interactions between transient eddies and the time mean flow. However, their domain averages are often of the same order of magnitude as the rate of change of domain-averaged eddy kinetic energy. Furthermore, significant wave-wave interactions appear to be associated with wave mode transitions. These interactions are either between low-frequency and high-frequency traveling waves or between traveling waves and thermal tides. The two types of nonlinear interactions differ in spatial patterns, and their relative importance also varies with specific transitions. This indicates that, for a simulation with diurnally averaged solar forcing, wave mode transitions will probably occur less frequently as the nonlinear interactions involving thermal tides are removed. Indeed,

Collins et al. (1995) found that simulations with diurnally averaged insolation developed highly regular transient eddies, while those with a diurnal cycle led to more irregular transient eddies that sporadically changed the dominant wave mode.

Acknowledgments

This paper is supported partially by NASA grant NNX10AB85G and partially by NASA grant NNX14AG55G. The computations were run on the Odyssey cluster supported by the Faculty of Arts & Sciences (FAS) Research Computing Group at Harvard University. The MACDA dataset used in Section 2 is downloaded from the British Atmospheric Data Centre (BADC) website.

References

- Banfield, D., Conrath, B.J., Gierasch, P.J., et al., 2004. Traveling waves in the martian atmosphere from MGS TES Nadir data. *Icarus* 170, 365–403.
- Basu, S., Wilson, R.J., Richardson, M.I., et al., 2006. Simulation of spontaneous and variable global dust storms with the GFDL Mars GCM. *J. Geophys. Res.* 111 (E9), E09004. doi:[10.1029/2005JE002660](https://doi.org/10.1029/2005JE002660).
- Barnes, J.R., 1980. Time spectral analysis of midlatitude disturbances in the martian atmosphere. *J. Atmos. Sci.* 37, 2002–2015.
- Barnes, J.R., 1981. Midlatitude disturbances in the martian atmosphere: A second Mars year. *J. Atmos. Sci.* 38, 225–234.
- Barnes, J.R., Pollack, J.B., Haberle, R.M., et al., 1993. Mars atmospheric dynamics as simulated by the NASA Ames general circulation model. 2. Transient baroclinic eddies. *J. Geophys. Res.* 98 (E2), 3125–3148 paper number 92JE02935.
- Benson, J.L., Kass, D.M., Kleinbohl, A., 2011. Mars' north polar hood as observed by the Mars Climate Sounder. *J. Geophys. Res.* 116, E03008. doi:[10.1029/2010JE003693](https://doi.org/10.1029/2010JE003693).
- Cantor, B.A., James, P.B., Caplinger, M., et al., 2001. Martian dust storms: 1999 Mars Orbiter Camera observations. *J. Geophys. Res.* 106 (E10), 23653–23687. doi:[10.1029/2000JE001310](https://doi.org/10.1029/2000JE001310).
- Collins, M., Lewis, S.R., Read, P.L., 1995. Regular and irregular baroclinic waves in a martian general circulation model – a role for diurnal forcing. *Adv. Space Res.* 16 (6), 3–7. doi:[10.1016/0273-1177\(95\)00243-8](https://doi.org/10.1016/0273-1177(95)00243-8).
- Collins, M., Lewis, S.R., Read, P.L., et al., 1996. Baroclinic wave transitions in the martian atmosphere. *Icarus* 120 (2), 344–357. doi:[10.1006/icar.1996.0055](https://doi.org/10.1006/icar.1996.0055).
- Hayashi, Y., 1982. Space-Time spectral analysis and its applications to atmospheric waves. *J. Meteorol. Soc. Jpn.* 60, 156–170.
- Hayashi, Y., Golder, D.G., 1983. Transient planetary waves by GFDL spectral general circulation models. Part II: Effects of nonlinear energy transfer. *J. Atmos. Sci.* 40, 951–957.
- Hinson, D.P., Smith, M.D., Conrath, B.J., 2004. Comparison of atmospheric temperatures obtained through infrared sounding and radio occultation by Mars Global Surveyor. *J. Geophys. Res.* 109, D12002. doi:[10.1029/2004JE002344](https://doi.org/10.1029/2004JE002344).
- Hinson, D.P., Wang, H., 2010. Further observations of regional dust storms and baroclinic eddies in the northern hemisphere of Mars. *Icarus*, 206 1, 290–305.
- Hinson, D.P., Wang, H., Smith, M.D., 2012. A multi-year survey of dynamics near the surface in the northern hemisphere of Mars: Short-period baroclinic waves and dust storms. *Icarus* 219, 307–320. doi:[10.1016/j.icarus.2012.03.001](https://doi.org/10.1016/j.icarus.2012.03.001).
- Hollingsworth, J.L., Haberle, R.M., Barnes, J.R., et al., 1996. Orographic control of storm zones on Mars. *Nature* 380, 413–416.
- Holton, J.R., Hakim, G.J., 2013. *An Introduction to Dynamic Meteorology*, 5 edition Academic Press.
- Kavalich Jr., M.J., Szunyogh, Gyarmati, G., Wilson, R.J., 2013. Local dynamics of baroclinic waves in the martian atmosphere. *J. Atmos. Sci.* 70, 3415–3447. doi:[10.1175/JAS-D-12-0262.1](https://doi.org/10.1175/JAS-D-12-0262.1).
- Laprise, R., 1992. The Euler equations of motion with hydrostatic pressure as an independent variable. *Mon. Wea. Rev.* 120, 197–207.
- Lewis, S.R., Mulholland, D.P., Read, P.L., et al., 2016. The solsticial pause on Mars: 1. A planetary wave reanalysis. *Icarus* 264, 456–464. doi:[10.1016/j.icarus.2015.08.039](https://doi.org/10.1016/j.icarus.2015.08.039).
- Määttänen, A., Listowski, C., Montmessin, F., et al., 2013. A complete climatology of the aerosol vertical distribution on Mars from MEX/SPICAM UV solar occultations. *Icarus* 223, 892–941. doi:[10.1016/j.icarus.2012.12.001](https://doi.org/10.1016/j.icarus.2012.12.001).
- Montabone, L., Marsh, K., Lewis, S.R., et al., 2014. The Mars analysis correction data assimilation (MACDA) dataset V1.0. *Geosci. Data J.* doi:[10.1002/gdj3.13](https://doi.org/10.1002/gdj3.13).
- Montabone, L., Forget, F., Millour, E., et al., 2015. Eight-year climatology of dust optical depth on Mars. *Icarus* 251, 65–95 <http://dx.doi.org/10.1016/j.icarus.2014.12.034>.
- Montmessin, F., Forget, F., Rannou, P., et al., 2004. Origin and role of water ice clouds in the martian water cycle as inferred from a general circulation model. *J. Geophys. Res.* 109, E10004 <http://dx.doi.org/10.1029/2004JE002284>.
- Mulholland, D.P., Lewis, S.R., Read, P.L., et al., 2016. The solsticial pause on Mars: 2. Modeling and investigation of causes. *Icarus* 264, 465–477. doi:[10.1016/j.icarus.2015.08.038](https://doi.org/10.1016/j.icarus.2015.08.038).
- Richardson, M.I., Toigo, A.D., Newman, C.E., 2007. PlanetWRF: A general purpose, local to global numerical model for planetary atmospheric and climate dynamics. *J. Geophys. Res.* 112, E09001 <http://dx.doi.org/10.1029/2006JE002825>.

- Sheng, J., Derome, J., 1991. An observational study of the energy transfer between the seasonal mean flow and transient eddies. *Tellus* 43A, 128–144.
- Smith, M.D., 2004. Interannual variability in TES atmospheric observations of Mars during 1999–2003. *Icarus* 167, 148–165.
- Toigo, A.D., Lee, C., Newman, C.E., et al., 2012. The impact of resolution on the dynamics of the martian global atmosphere: Varying resolution studies with the MarsWRF GCM. *Icarus* 221 (1), 276–288.
- Ulbrich, U., Speth, P., 1991. The global energy cycle of stationary and transient atmospheric waves: Results from ECMWF analysis. *Meteorol. Atmos. Phys.* 45, 125–138.
- Wang, H., Ingersoll, A.P., 2002. Martian clouds observed by Mars Global Surveyor Mars Orbiter Camera. *J. Geophys. Res.* 107, E10. doi:[10.1029/2001JE001815](https://doi.org/10.1029/2001JE001815), Art. No. 5078.
- Wang, H., Richardson, M.I., Wilson, R.J., et al., 2003. Cyclones, tides and the origin of major dust storms on Mars. *GRL* 30 (9), 1488. doi:[10.1029/2002GL016828](https://doi.org/10.1029/2002GL016828).
- Wang, H., Zurek, R.W., Richardson, M.I., 2005. The Relationship between frontal dust storms and transient eddy activity in the northern hemisphere of Mars as observed by Mars global surveyor. *J. Geophys. Res.* 110 (E7), E07005. doi:[10.1029/2005JE002423](https://doi.org/10.1029/2005JE002423).
- Wang, H., 2007. Dust storms originating in the northern hemisphere during the third mapping year of Mars Global Surveyor. *Icarus* 189 (2), 325–343. doi:[10.1016/j.icarus.2007.01.014](https://doi.org/10.1016/j.icarus.2007.01.014).
- Wang, H., Richardson, M.I., Toigo, A.D., et al., 2013. Zonal wavenumber three traveling waves in the northern hemisphere of Mars simulated with a general circulation model. *Icarus* 223, 654–676 <http://dx.doi.org/10.1016/j.icarus.2013.01.004>.
- Wang, H., Richardson, M.I., 2015. The origin, evolution, and trajectory of large dust storms on Mars during Mars years 24–30 (1999–2011). *Icarus* 251, 112–127. doi:[10.1016/j.icarus.2013.10.033](https://doi.org/10.1016/j.icarus.2013.10.033).
- Wilson, R.J., Banfield, D., Conrath, B.J., et al., 2002. Traveling waves in the northern hemisphere of Mars. *GRL* 29 (14), 1684. doi:[10.1029/2002GL014866](https://doi.org/10.1029/2002GL014866).